WELDING RESEARCH

SUPPLEMENT TO THE *WELDING JOURNAL*, DECEMBER 2006
Sponsored by the American Welding Society and the Welding Research Council

Simulation of Weld Pool Dynamics in the Stationary Pulsed Gas Metal Arc Welding Process and Final Weld Shape

A computer simulation accurately predicts weld pool fluid flow convection and final weld shape

BY M. H. CHO, Y. C. LIM, AND D. F. FARSON

ABSTRACT. The pulsed gas metal arc welding (GMAW-P) process was modeled numerically using a code based on the volume of fluid (VOF) technique, chosen primarily for its ability to accurately calculate the shape and motion of free fluid surfaces, which is needed for subsequent study of welding phenomena such as bead hump formation, incomplete fusion in narrow groove welds, and weld toe geometry. According to the mathematical models with parameters obtained from analysis of high-speed video images and data acquisition (DAQ) system, GMAW-P was simulated and then validated by comparison of measured and predicted weld deposit geometry, transient radius, and temperature history. Based on the weld simulation parameters, a parametric study of weld simulation was performed to demonstrate and understand the effectiveness of individual simulation parameters on heat and fluid flow in the molten weld pool and the final configuration of stationary welds. Constricted current density drastically increased the weld penetration and decreased the weld radius, primarily by reducing the convexity of the weld deposit and promoting heat transfer to the bottom of the weld pool. Conversely, decreased arc force and increased arc pressure radius both decreased the weld penetration for the same reason. Based on the understanding of weld pool spreading, GMAW-P was simulated with an additional heat source to demonstrate the utility of the simulation in predicting final weld shape in complex welding situations.

M. H. CHO(ch.130@osu.edu) *is postdoctoral researcher, Y. C. Lim (lim.746@osu.edu) is graduate research associate, and D. F. Farson* (farson.4@osu.edu)*is associate professor, Department of Industrial, Welding and Systems Engineering, The Ohio State University, Columbus, Ohio.*

Introduction

During arc welding processes such as gas metal arc welding (GMAW) and gas tungsten arc welding (GTAW), fluid flow and heat flow are key factors that determine the final weld shape. Therefore, many previous efforts have been made to predict these two aspects of arc welding by numerical simulation. While currently available welding heat flow and distortion simulations are quite comprehensive and accurate enough for many practical purposes, phase change and fluid flow phenomena occurring in arc welding are complex and have still not been realistically simulated. In particular, numerical model-based prediction of the dynamic changes in the shape of the liquid weld pool surface would be useful in many applications if they were possible. Examples include weld toe shape (Ref. 1) and weld bead hump formation (Ref. 2).

In GMAW, heat input to the weld pool is composed of a direct arc heat input and the enthalpy of molten droplets transferring from the welding wire. In numerical weld pool simulations, the current density is also needed to predict the distribution of Lorentz force in the weld pool fluid. These parameters are difficult to measure for GMAW because of difficulties posed by filler metal transfer, but measurements have been made for GTAW. To quantify direct heat and also the electrical current distributions on the weld pool surface, Lu and Kou (Ref. 3) measured power and current density distributions using a split copper block. Based on the analysis by the Abel inversion method, the shape of power and current distribution were found out to be Gaussian density functions, so the arc shape could be described by the total magnitudes (i.e., total heat input and current) and Gaussian distribution parameters.

The shape of the weld pool and bead shape are also strongly affected by the flow of plasma in the welding arc. The forces exerted by the arc plasma jet on the weld pool are the arc stagnation pressure and drag force. Arc pressure acts on the weld pool surface in the normal direction, depressing the molten deposit. Arc pressure density distribution on the weld pool surface has also been investigated for GTAW (Ref. 4), and was characterized as a Gaussian density distribution function. Adonyi et al. (Ref. 5) studied its effect on the weld pool dynamics and found that the arc pressure mainly caused the depression of the weld pool surface. Drag force is a shear stress on the liquid metal surface produced by plasma gas flow. Tanaka et al. (Ref. 6) investigated the driving forces for weld pool convection during gas tungsten arc welding, and the drag force and the Marangoni force (discussed below) were

KEYWORDS

3-D Numerical Simulation
Fluid Flow
Heat Flow
Pulsed GMAW
Volume of Fluid
Weld Shape
Weld Simulation

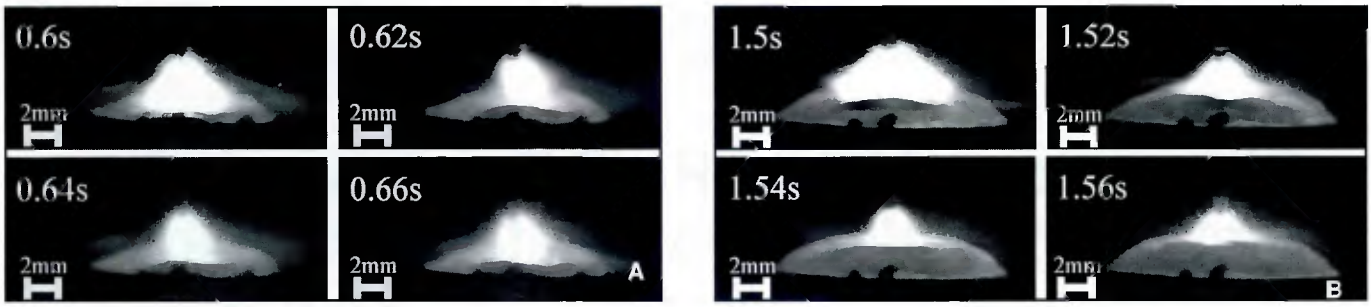

Fig. 1 — High-speed video sequences showing different metal transfer of molten droplets at later times.

Fig. 2 — Images of electrode tip used to measure the tip taper angles.

found to be dominant. Convection caused by surface tension gradients has major effects (Ref. 3) on weld pool shape. The mechanism was studied by Heiple and Roper (Refs. 7, 8). They proposed that the final weld shape can be significantly altered by variations of the surface active elements (e.g., sulfur) that changes the direction of surface tension gradient induced flow (Marangoni flow) in GTA welding conditions.

Based on understanding the well-known forces and heat input in the weld pool, many researchers simulated arc welding processes and studied weld pool convection, the formation of the weld pool and molten droplets, droplet transfer, and solidified weld bead shape. The idea of solving for the shape of the free surface of a fluid volume as a static energy minimization problem (Ref. 9) has been applied to calculate weld bead shape by a number of authors (Refs. 10–14). Zhang et al. (Refs. 15–17) studied the three-dimensional numerical simulation of the complex geometry such as fillet welds based on the surface energy minimization for the surface deformation tracking. Also, Kumar and DebRoy (Ref. 18) developed optimization algorithm to minimize the error between the experimental results and the simulation results by the determination of unknown variables from a limited volume of experimental data.

Since the molten weld metal is not stationary and is also cooling and solidifying as it accumulates and spreads to form a weld bead, a more accurate analysis of bead shape takes simultaneous fluid and heat flow into account in addition to the forces included in the static balance. Trapaga and Szekely (Ref. 19) used the VOF numerical technique to simulate the isothermal spreading of impacting droplets on surfaces. Zheng (Ref. 20) modeled the spreading of an impacting droplet using the level set method, another interface tracking scheme with similarities to VOF. Wang and Tsai (Ref. 21) investigated the dynamics of periodic filler droplets impinging onto weld pool and phase change, using VOF technique that can handle a transient deformed weld pool surface and the continuum model (Ref. 22), respectively.

More recently, the VOF technique has been used to simulate melting and detachment of metal droplets from welding wire in GMAW (Refs. 23–28), and Fan and Kovacevic (Ref. 29) developed the unified two-dimensional axisymmetric model to study droplet formation and detachment, droplet transfer in arc plasma, impingement of droplets on the weld pool, and solidification in gas metal arc welding.

In summary, GMAW simulations using the VOF technique in the previous research papers were limited to a two-dimensional axisymmetric model, which is not useful in most welding applications. Also, arc pressure and drag force on the weld pool surface induced by plasma gas flow were neglected, which is very significant when the welding current is high enough to generate the spray metal transfer mode.

In this article, a three-dimensional numerical simulation of a high peak current GMAW-P using the VOF method is developed based on mathematical models, especially including arc pressure and plasma drag force, obtained from the previous research papers. In order to arrive at a GMAW-P simulation that can be executed in a relatively short time and is also accurate enough for engineering use, the arc effects were represented as boundary and body inputs. Thus, simulation parameters to characterize the molten filler metal droplets and arc dimensions were measured from experiments. Also, the real-time weld pool radius measurements, thermal history measurements at selected positions, and cross sections of final weld

Table 1 — Thermophysical Material Properties of A36 Used in the Simulation

Density	7800 kg/m^3	Thermal expansion coefficient	14.4 x 10^{-6} m/m K
Dynamic viscosity	6 x10^{-3} kg/m s	Liquidus temp.	1798 K
Thermal conductivity (s)	Temp. dependant	Solidus temp.	1768 K
Thermal conductivity (1)	26W/m K	Vaporized temp.	2900 K
Specific heat (s)	686 J/kg K	Heat transfer coefficient	100 W/m^2 K
Specific heat (1)	866 J/kg K	Emissivity	0.5
Latent heat of fusion	2.77 x 10^{5}J/kg	Material permeability	1.26 x 10^{-6} H/m
Latent heat of vaporization	7.34 x 10^6 J/kg	Drag coefficient constant	1

Table 2 — Pulsed GMAW Current Waveform and Welding Parameters

Peak current	384 A	Instantaneous avg. power	8842 W
Background current	87.4 A	Wire feed speed (WFS)	148 mm/s
Peak voltage	35.5 V	Welding wire type	ER70S-6
Background voltage	24.4 V	Wire diameter	1.125 mm
Pulse time	2.2 ms	CTWD	19.05 mm
Pulse frequency	250 Hz	Shielding gas/flow rate	Ar,10CO_2/40 ft^3/h

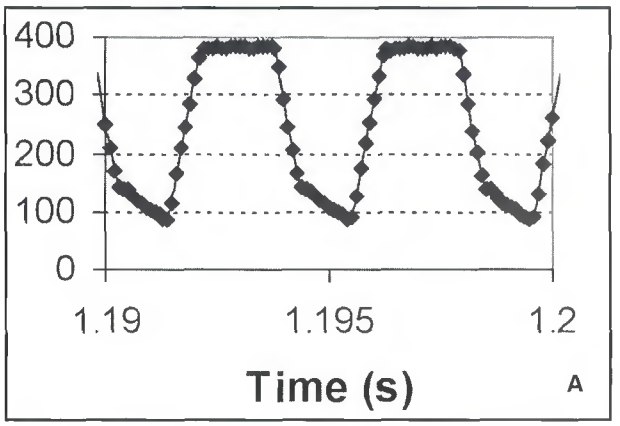

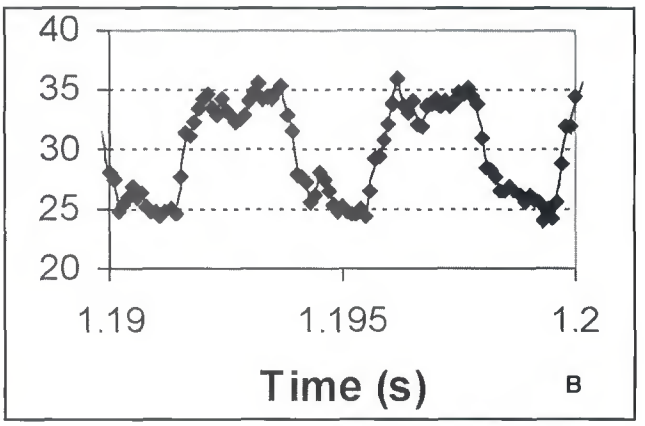

Fig. 3 — GMAW-P. A — Current waveform; B — voltage waveform.

profiles and fusion boundaries were used for simulation validation. The effects of selected individual simulation parameters on GMA weld pool flow and final weld shape were also investigated.

Finally, predictions of the transient and final weld shape for a dual heat source process influence are shown to illustrate the usefulness of the simulation for welding process development, which cannot be simulated using a two-dimensional axisymmetric model.

Experimental Procedure

Stationary welds were made for 1.8 s using the pulsed gas metal arc welding process (using a Thermal Arc 500P power supply). Materials selected for the experiment were 6.35-mm-thick ASTM A-36 steel, containing 50 ppm sulfur, with sandblasted surface preparation for the workpiece and 1.143 mm diameter of ER70S-6 welding wire. Contact-tip-to-work distance (CTWD) was 19.1 mm. Thermophysical material properties of A-36 steel are shown in Table 1.

During the welds, measurements were made with a high-speed CCD camera and a data acquisition system (DAQ). Images of the arc and molten metal pool were captured by the high-speed CCD camera with a 950 nm ±10 nm band pass filter mounted between high-speed camera lenses used to filter out unwanted arc light in order to capture the clear images of metal transfer and weld deposit growth. According to video images of metal transfer (Fig. 1), one drop per pulse metal transfer was observed after 1.2 s of weld time. Before that time, the molten metal transfer was somewhat random but the transfer rate was approximately one drop every two pulses. It is supposed that this difference in transfer corresponds to differences in the temperature distribution in the welding wire extension. The arc length measured from the arc images was approximately 4 mm.

As shown in Fig. 2, the electrode tip was relatively blunt at the beginning of the weld, but became sharper when the metal transfer stabilized. The tip angle was measured to be approximately 90 deg before 1.2 s and 60 deg after 1.2 s. The transient weld deposit profile and radius were measured from images taken at 500 frames per second.

The velocity of molten droplets was too high to analyze at the 500 frames per second rate, so the recording rate was increased to 4500 frames per second to analyze their size and speed.

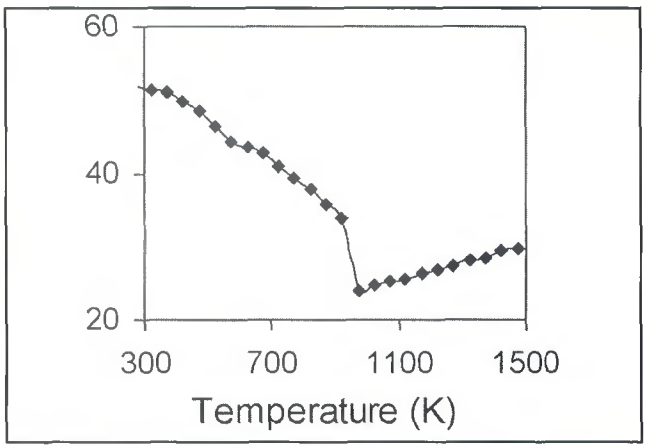

Fig. 4 — Temperature vs. thermal conductivity used in the simulations.

Welding current and voltage waveforms were acquired at a sampling rate of 10 kHz. Examples of the waveforms are shown in Fig. 3. Peak values and background values of current and voltage, pulse frequency, and pulse duration were obtained from the waveforms and used to calculate the instantaneous average power, peak power, and background power for the heat input in the weld system during the process. The waveform parameters and welding parameters are displayed in Table 2.

Mathematical Modeling and Numerical Simulation

The GMAW-P weld pool and bead deposit were mathematically modeled using 3-D Cartesian coordinate system, and the governing equations were solved numerically to simulate the arc welding process using Flow3D commercial code. The liquid metal was considered to be an incompressible Newtonian fluid, and flow was laminar. The density change of molten metal was only considered for the buoyancy term in the momentum equation using a Boussinesq approximation. The flow at the solid/liquid phase interface was modeled using a porous media drag concept (Ref. 39). Arc heat input (defined as the direct heat input to the workpiece) and arc pressure on the molten pool surface were modeled as Gaussian density distributions. The total heat input applied to the workpiece, calculated by multiplying the instantaneous average arc power by a process efficiency, was the sum of direct heat input and the latent heat of droplets.

The weld pool simulation was based on the numerical solution of mass, momentum, and energy conservation relationships

$$B = -\frac{1}{\rho}\left(\frac{2\rho}{2t}\right) \quad (1)$$

$$\frac{\partial \mathrm{v}}{\partial t} + \mathrm{v}\cdot\nabla\mathrm{v} = -\frac{1}{\rho}\nabla P + \nu\nabla^2\mathrm{v} + f + \frac{\dot{m}_s}{\rho}\cdot\mathrm{v} - K\mathrm{v} \quad (2)$$

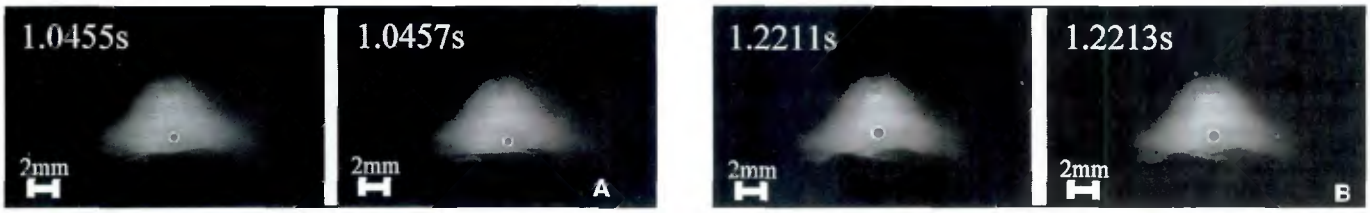

Fig. 5 — Drop velocity measurement. A — For one drop per every two pulses (125 Hz); B — one drop per pulse (250 Hz).

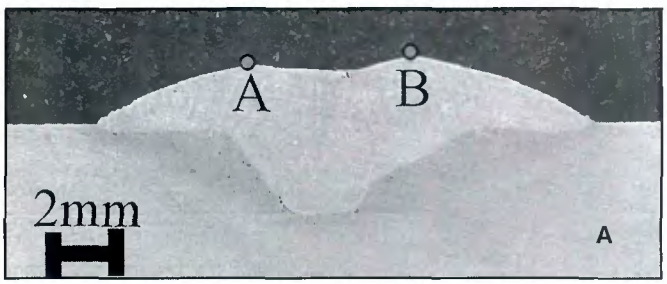

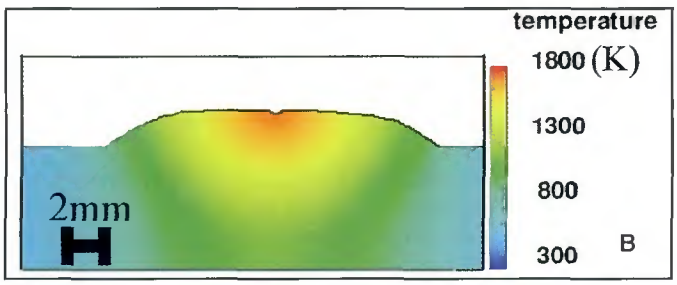

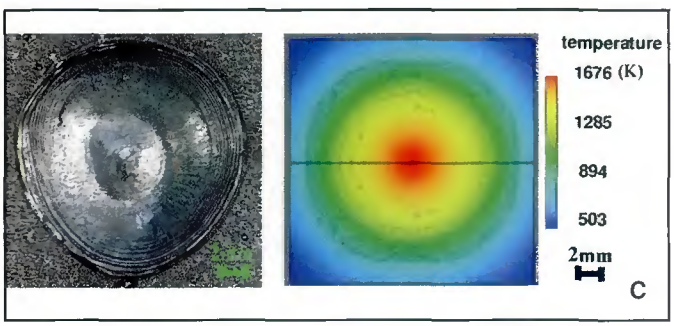

Fig. 6 — A — Cross sections of actual weld; B — simulated weld after the solidification of weld; C — top views of the weld for the experiment and the simulation.

$$\rho\left(\frac{\partial U}{\partial t}+\mathrm{v}\bullet\nabla U\right)=\nabla\bullet(k\nabla T)+\dot{U}_s \qquad (3)$$

where v is molten metal velocity, $\dot{m}_s$ is a mass source term, P is hydrodynamic pressure, v is kinematic viscosity, f is body accelerations due to body force (e.g., gravity acceleration), ρ is a fluid density, K is the drag coefficient for a porous media model, U is internal energy per unit mass, k is thermal conductivity (temperature-dependent values), T is a local temperature and, $\dot{U}_s$ is an energy source term due to a mass source term.

To model solid-liquid phase changes, the mathematical model of enthalpy-temperature relationship is

$$h=\begin{cases}\rho_s C_s T & (T\le T_s)\\ h(T_s)+h_{sl}\dfrac{T-T_s}{T_l-T_s} & (T_s<T\le T_l)\\ h(T_l)+\rho_l C_l(T-T_l) & (T_l<T)\end{cases} \qquad (4)$$

where h is enthalpy, ρ_s and ρ_l are solid and liquid density, respectively, C_s and C_l are specific heat at constant volume of the solid and liquid phases, T_s and T_l are solidus and liquidus temperatures of the metal alloy, and h_{sl} is the latent heat of fusion for phase change between liquid and solid.

The simulation technique used in this work is based on an additional advection relationship that expresses the conservation of volume fraction in the fluid flow at the free surface and fluid interfaces (for a two-fluid model). It is derived from the conservative form of the mass conservation law using density and fluid volume fraction relationships

$$\frac{\partial\rho}{\partial t}+\nabla\bullet(\mathrm{v}\rho)=\dot{m}_s \qquad (5)$$

$$\rho=\rho_o F \qquad (6)$$

$$\dot{m}_s=\rho_o\dot{F}_s \qquad (7)$$

where ρ is the zone density at the current cell, ρ_o is the density of material, F is a volume fraction of a fluid, and $\dot{F}_s$ represents the change of the volume fraction of fluid associated with the mass source m_s in the continuity equation. Substituting Equations 6 and 7 into 5 results in the volume of fluid (VOF) Equation 8, which can be used to effectively track the location of free fluid surfaces in the simulation domain.

$$\frac{\partial F}{\partial t}+\nabla\bullet(\mathrm{v}F)=\dot{F}_s \qquad (8)$$

Based on Equation 8, free surface cells are defined as those that have void (zero volume fraction) neighbor cells. A numerical technique for tracking the shape and volume of the free surface of fluid and a volume advection algorithm presented by Hirt and Nichols (Ref. 30) is not reiterated here.

Since a single fluid is used in the model, the solid and liquid phases are distinguished based on the enthalpy-temperature relationship (Equation 4). The fluid temperature of each cell is determined from its enthalpy, which is computed based on conduction and convection of material. If the temperature is between liquidus and solidus temperatures, the cell becomes a part of a mushy zone. The amount of solid phase is calculated in terms of the temperature ratio and is used for the determination of the effective viscosity and the drag coefficient in the mushy zone.

To model flow in the mushy zone, it is divided into three subregions distinguished by the critical solid fraction and the coherent solid fraction. Fluid in each subregion is assigned a different drag coefficient and a local viscosity. The first region consists of cells with solid fraction below the coherent solid fraction. The local viscosity is varied due to the amount of solid fraction according to

$$\mu=\mu_0\left(1-\frac{F_s}{F_{cr}}\right)^{-1.55} \qquad (9)$$

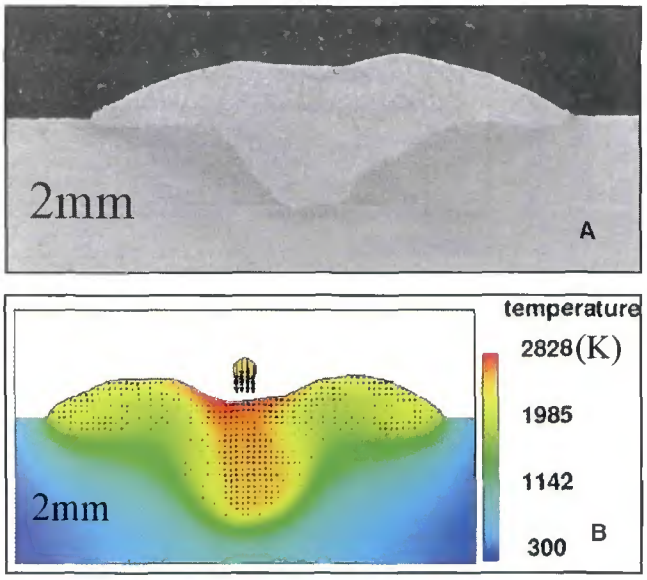

Fig. 7 — A — Cross sections of actual weld; B — simulated weld at the arc termination time. Simulated penetration is deeper than actual weld.

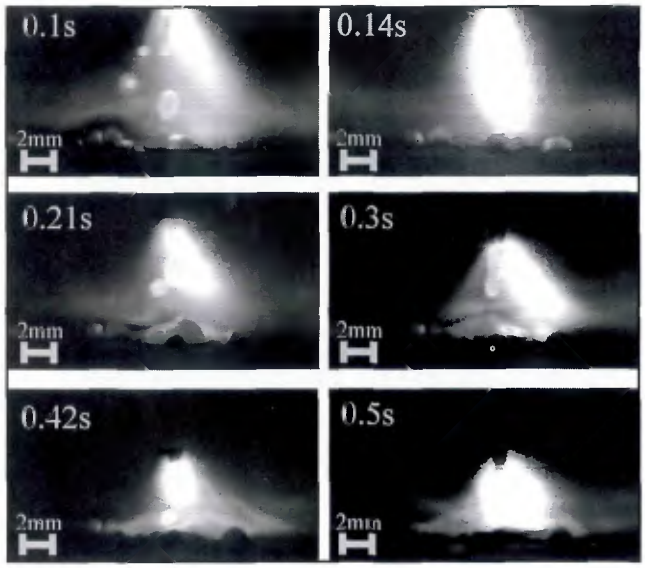

Fig. 8 — High-speed video sequences showing erratic initial metal transfer of molten droplets.

Table 3 — The Summary of Weld Geometry from the Experimental Results and the Simulation

Deposit Characteristics	Measured	Simulated	Difference
Height	2.3/1.9 mm	1.88 mm	0.42/0.02 mm
Average radius	8.25 mm	8.5 mm	0.25 mm
Center penetration	3.2 mm	4.6 mm	1.4 mm
Edge penetration	0.5 mm	0.6 mm	0.1 mm
Left-side toe angle	30.4 deg	31.8 deg	1.4 deg
Right-side toe angle	32.6 deg	33.2 deg	0.6 deg

where μ_0 is dynamic viscosity, F_s is the local solid fraction in the given cell, and F_{cr} is the critical solid fraction.

The second region of the mushy zone consists of cells where the solid fraction is above the coherent solid fraction but less than the critical solid fraction. In this region, the microstructure is acting as a porous media so the Carman-Koseny equation (Ref. 31) that is derived from Darcy model (Refs. 32, 33) is used to compute the drag coefficient

$$K = C_o \cdot \frac{F_s^2}{(1-F_s)^3 + \varepsilon} \quad (10)$$

where K is the drag coefficient, C_o is the drag coefficient constant (equal to 1 for steel), and ε is the positive zero (for computation purposes). In this region, Equation 9 is still needed to calculate the local viscosity of fluid to compute the precise fluid resistance in the computational cell.

In the region above the critical solid fraction, the microstructure is assumed to be fully developed into a complete rigid structure, and there is assumed to be infinite resistance to fluid flow. Thus, fluid flow is stopped due to an effectively infinite drag coefficient computed by Equation 10.

Boundary Conditions

The axisymmetric free surface heat input from the arc was modeled as a fixed Gaussian density function (Ref. 34).

$$q(r) = \frac{Q}{2\pi\sigma_a^2} \exp\left(\frac{-r^2}{2\sigma_a^2}\right) \quad (11)$$

where Q is the actual heat input directly from the arc to the substrate and σ_a is the Gaussian heat distribution parameter. The Gaussian heat distribution parameter is the main factor to adjust the heat input distribution on the free surface of the weld pool. Additionally, convection and radiation are applied on the free surface. Therefore, the heat input on the free surface is expressed as

$$q(r) = \frac{Q}{2\pi\sigma_a^2} \exp\left(\frac{-r^2}{2\sigma_a^2}\right) - h_c(T - T_0) - \sigma\varepsilon\left(T^4 - T_0^4\right) \quad (12)$$

where h_c is heat transfer coefficient, T is temperature. T_0 is ambient temperature, σ is the Stefan-Boltzmann constant (5.67×10^{-8} W/m^2• K^4), and ε is the emissivity. The wall boundary condition was applied to solid free surface cells

$$-k\frac{\partial T}{\partial n} = -h_c(T - T_0) \quad (13)$$

To model Marangoni flow, the shear stress balance as boundary condition on the free surface is described as

$$\mu\frac{\partial v_t}{\partial n} = -\frac{\partial \gamma}{\partial T}\frac{\partial T}{\partial r} \quad (14)$$

where μ is the dynamic viscosity, v_t is the tangential velocity vector, n is the normal to the free surface, $\partial\gamma/\partial T$ is the surface tension gradient, and r is the tangential direction on the free surface. An additional plasma drag shear stress is described below. Also, the normal pressure balance as boundary condition on the free surface is expressed as

$$-p + 2\mu\frac{\partial v_n}{\partial n} = -p_{arc} + \gamma\left(\frac{1}{R_1} + \frac{1}{R_2}\right) \quad (15)$$

where p is the liquid pressure at the free surface in the normal direction, v_n is the normal velocity vector, p_{arc} is the arc pressure (described below), γ is the surface

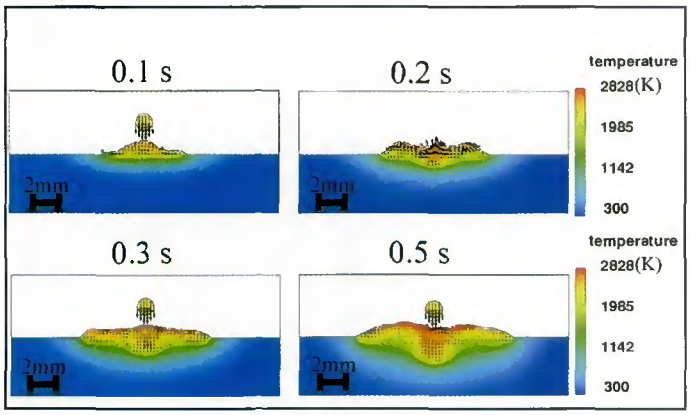

Fig. 9 — Cross-section views of the simulated weld at early weld times showing the progress of the fluid flow development and the weld penetration.

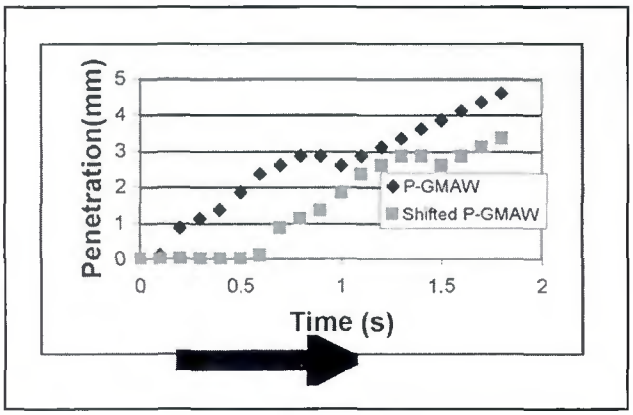

Fig. 10 — Simulated weld penetration vs. time showing a shift of about 0.5 s matched experimental measurements.

tension, and R_1 and R_2 are the principal radii of surface curvature. For this study, surface tension is obtained from the formula developed by Sahoo et al. (Ref. 35). The equation of surface tension as a function of temperature with sulfur active element in a binary Fe-S system is expressed by

$$\gamma(T)=\gamma_m^o - A\bullet(T-T_m) - R\bullet T\bullet\Gamma_s\bullet\ln\left(1+k_1\bullet a_i\bullet e^{-\Delta H^o/RT}\right) \quad (16)$$

where γ^o_m is the surface tension of pure metal at the melting point, 1.943, A is the negative of surface tension gradient for pure metal, 4.3E-4, T_m is the melting point of the material, 1798 K, R is gas constant, Γ_s is the surface excess at saturation, 1.3E-8, k_1 is the entropy factor, 0.00318, a_i is weight percent of sulfur, 0.005%, and ΔH_o is the heat of absorption, –1.66E+8. According to Equation 16, the negative surface tension gradient at temperatures above 2000 K is large so a strong outward Marangoni force spreads the molten metal.

Pressure gradients generated by Lorentz force in the arc plasma causes downward (along the negative z-coordinate) flow of the ionized gas. A stagnation pressure that is consistent with the redirection of this downward flow is approximated as Gaussian density distribution whose magnitude and radius are based on analysis of experimental results (Ref. 4)

$$p_{arc}(r)=\frac{P}{2\pi\sigma_p^2}\exp\left(\frac{-r^2}{2\sigma_p^2}\right) \quad (17)$$

where σ_p is Gaussian pressure distribution parameter and P is total force (N).

When the plasma jet flow impinges on the weld pool surface, the plasma drag force is induced on the weld pool surface. This plasma drag force creates outward fluid flow of liquid metal at the surface and also changes with weld pool configuration. In this work, an analytical solution (Ref. 36) of the wall shear stress produced by the normal impingement of a plasma jet on a flat surface was used to determine and apply the drag force as the boundary condition on the free surface cell. For the axisymmetric case, the theoretical equation in terms of Reynolds number, a ratio of jet height, and nozzle diameter, is expressed as

$$\frac{\tau}{\rho_p u_o^2}\mathrm{Re}_o^{1/2}\left(\frac{H}{D}\right)^2 = g_2\left(\frac{r}{H}\right) \quad (18)$$

where τ is shear stress (N/m^2), ρ_p is plasma density (Kg/m^3), u_o is the initial plasma velocity (m/s), Re_o is Reynolds number, H is a nozzle height (m), D is the nozzle diameter (m), r is the radius (m) from the center, and g_2 is the universal function plotted in reference paper (Ref. 36). The initial plasma jet velocity is calculated based on the maximum plasma stagnation pressure at the weld pool center using Bernoulli's equation in order to obtain Reynolds number. The jet height and the jet nozzle diameter are assumed to be the arc length and the electrode size. The computed drag force is applied into the free surface cells as a body force in the momentum Equation 2.

A key feature of the simulation is the representation of melting of the GMA welding wire and the transfer of resulting droplets to the weld pool. Welding wire melting was modeled as a periodic stream of spherical droplets with velocity vectors in the negative z direction. Conservation of mass was applied to calculate the initial droplet radius from welding wire diameter and welding parameters (wire feed speed and drop frequency). The initial velocity of spherical droplets was directly measured from sequential arc images. Many researchers add the plasma drag force to the transferring droplets, computed as a function of droplet radius, drag coefficient for a sphere, and the plasma gas velocity in momentum equation, acting on the liquid droplet between the electrode tip and the base metal. In this model, the velocity of liquid droplet right before impinging on the weld pool was measured and used as the initial velocity of liquid droplet, and also the height of liquid droplet is fixed with respect to the free surface of the weld pool to maintain the same condition when measuring the velocity of liquid droplet. Due to the small traveling distance of the liquid droplet, the model assumes that the plasma drag force exerting on the liquid droplet can be ignored.

Body Forces in the Weld Pool

The body force term in momentum Equation 2 was comprised of the sum of two terms $\mathbf{f} = \mathbf{f}_b + \mathbf{f}_L$ where $\mathbf{f}_b$ is buoyancy force and $\mathbf{f}_L$ is Lorentz force. For the buoyancy force term, Boussinesq approximation concept was applied to account for the effect of a small density change in the gravity term

$$\mathrm{f}_b = -\beta\bullet(T-T_0)g \quad (19)$$

where $B=-\frac{1}{p}(\frac{2p}{2t})_p$ is the thermal expansion coefficient.

Lorentz force was obtained from an analytical solution (Refs. 37, 38) based on the current flow and associated magnetic field in the substrate material. The electric field is assumed to be quasi-steady state, the electrical conductivity is assumed to be constant and the material domain is a semi-infinite plate. Then, the electric potential field ϕ in the weldment is given by Laplace's equation

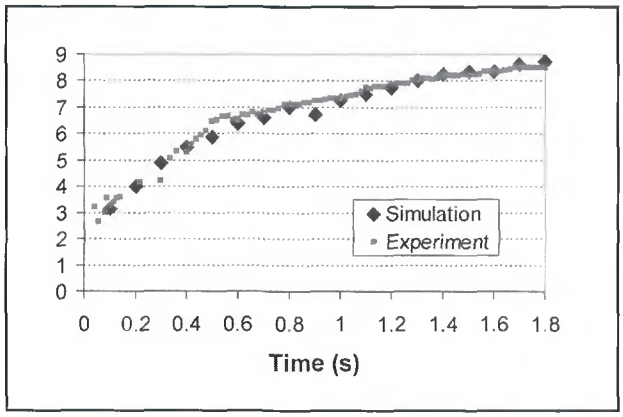

Fig. 11— Measured radius and simulated radius of weld deposits showing good correspondence.

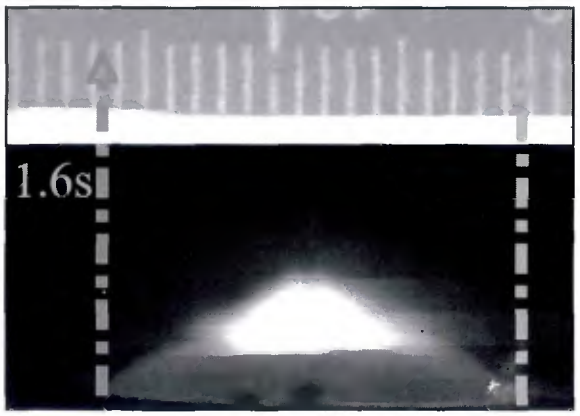

Fig. 12 — The sample of captured images showing the measurement of weld pool radius at 1.6 s weld time.

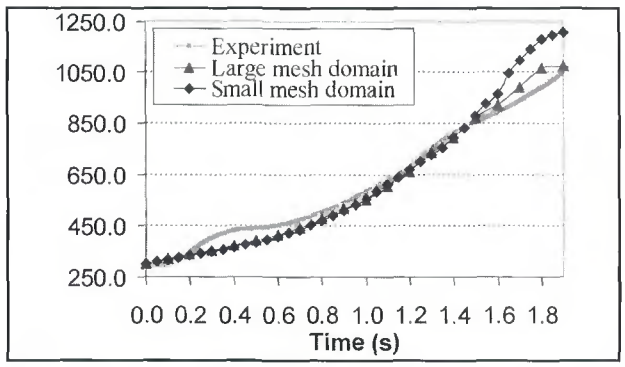

Fig. 13 — Temperature history measured at a location 0.4 mm away from the final weld edge and the predicted temperature for two different mesh domain sizes.

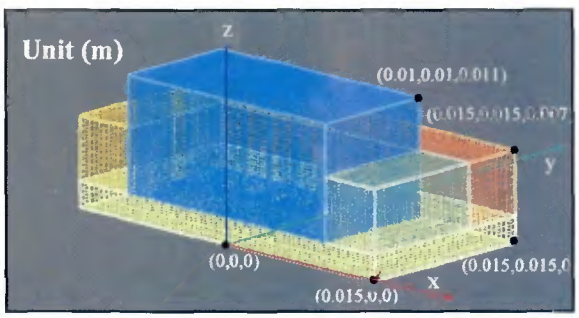

Fig. 14 — Coordinates of large mesh used for half symmetry simulation of stationary spot welds.

$$\nabla^2\phi = \frac{1}{r}\frac{\partial}{\partial r}\left(r\frac{\partial\phi}{\partial r}\right) + \frac{\partial^2\phi}{\partial z^2} = 0 \qquad (20)$$

The axisymmetric solution of Equation 20 is obtained using a Hankel transformation with boundary conditions

$$J_z(r,0) = -\sigma_e\frac{\partial\phi}{\partial z} = \frac{I}{2\pi\sigma_c^2}\exp\left(\frac{-r^2}{2\sigma_c^2}\right)$$

$$\frac{\partial\phi}{\partial z}(r,c) = 0 \qquad \frac{\partial\phi}{\partial r}(0,z) = 0 \qquad \frac{\partial\phi}{\partial r}(\infty,z) = 0 \qquad (21)$$

where σ_e is the electrical conductivity of the weld metal, σ_c is the Gaussian current parameter (m), I is a current (A), and c is the thickness of the workpiece. Note that the current distribution on the top of the free surface of the material is also described as Gaussian distribution function. This Gaussian distribution is varied as a function of the welding current and the Gaussian current parameter.

The two-dimensional axisymmetric Lorentz force must be converted to three-dimensional Cartesian coordinates for substitution into the momentum equation. The r and z Lorentz force components were calculated for the individual cells in 3-D Cartesian coordinate system based on the analytical solution. The r direction component was then split into x and y components.

Numerical Simulation

To perform the numerical simulation of the welding process, two regions, void and fluid, were generated in the computational domain with the fluid representing the material with the phase change capability. Due to weld pool surface deformation during the welding process, free surface modeling is applied to track the deformed free surface. In the fluid region either solid or liquid, governing Equations 1–4 and 8 with the required boundary conditions are numerically solved through the following steps (Ref. 39):

First, the new velocities at the current time level are approximated using the explicit method based on variables for the previous time level.

Second, the pressure correction formula (Poisson equation) was solved by the successive overrelaxation (SOR), method to satisfy the continuity equation and then the energy equation is solved by the implicit method.

Finally, the configuration of the free surface is updated using the VOF equation. These steps are repeated at every time step until the desired simulation time is reached.

There are four free surface boundary conditions to implement the effects of the electric arc on the weld pool — arc heat input, arc pressure, drag force, and drop generation. To numerically apply Gaussian heat flux on the free surface, the free surface cells were tracked, and at every time step an appropriate increment is added to their stored energy. The source term ($\dot{U}_s$) in energy Equation 3 is used to add the calculated thermal energy into the free surface cells. Also, the Gaussian arc stagnation pressure is numerically implemented in the momentum Equation 2 as a boundary condition at free surface. The corresponding pressure acts on the surface-normal direction on fluid in cells on the weld pool surface. Similarly, plasma drag force calculated from the theoretical equation as a function of the maximum pressure and the distance from the arc center is applied on the momentum Equa-

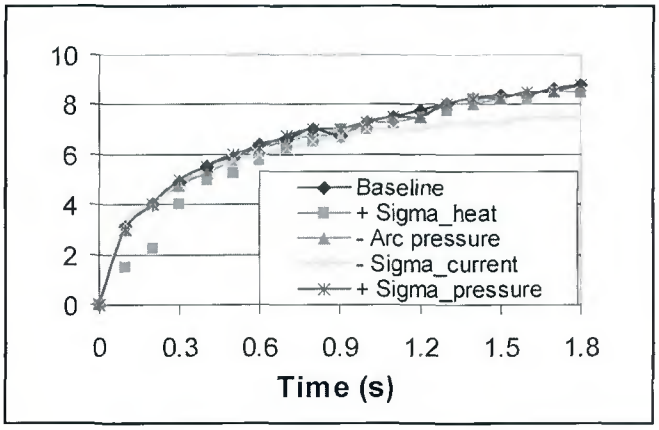

Fig. 15 — Comparison of the transient radius showing that increased heat input distribution radius slowed initial spreading and decreased current distribution radius slowed spreading at later times.

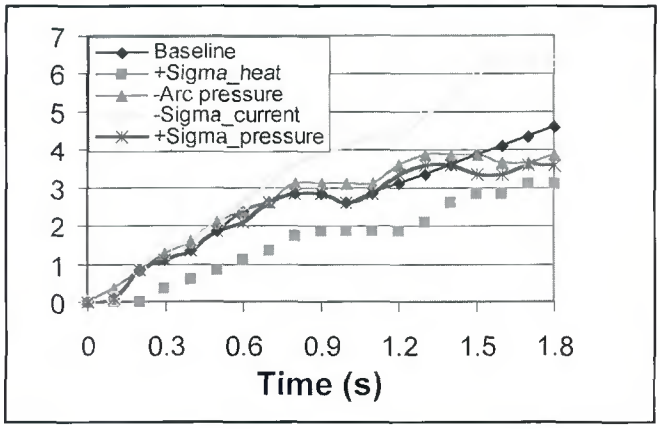

Fig. 16 — Comparison of transient weld penetration showing that increased heat and pressure input distribution and reduced arc pressure all decreased the final weld penetration while decreased current distribution radius caused deeper weld penetration.

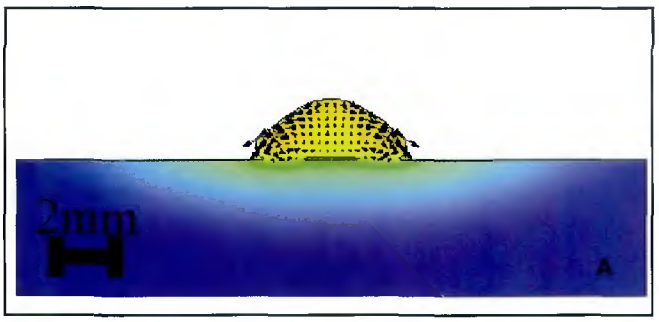

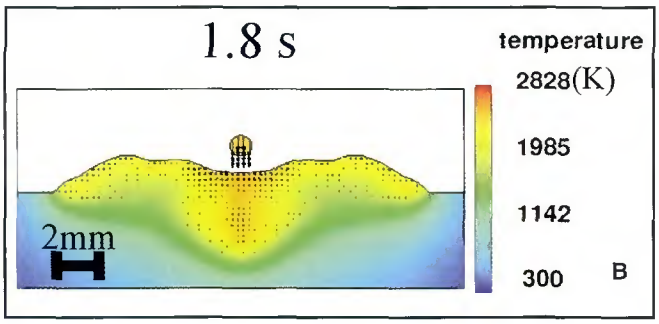

Fig. 17 — A — Cross section at the initial weld time showing arrest of molten metal spreading; B — at the later weld time showing the temperature distribution in the weld pool for the large Gaussian heat distribution parameter case.

tion 2 for the free surface cells.

Terms were added to all governing equations to model the generation of molten droplets in the void region. To add the mass of droplet, source terms in governing Equations 1 and 5 are modified to create the droplet, and then the momentum equation is used to set the initial velocity of the molten metal droplet and their height with respect to the free surface of a weld pool. In the energy Equation 3, the initial temperature of droplets (Refs. 40, 41) is used to calculate the amount of enthalpy that deposits into cells that correspond to droplet locations.

Simulation Parameters

The simulation parameters for Gaussian heat input, arc pressure, drag force, drop generation, and other physical parameters needed to conduct GMAW-P stationary weld simulations were based on current and voltage waveforms, video images of weld pool and metal transfer, and values from literature. Details of the parameters and measurements are summarized below.

Temperature-dependent thermal conductivity for the solid phase, shown in Fig. 4, was used to accurately evaluate the thermal diffusion. For the generalized solidification model (Ref. 42), the coherent solid fraction (0.48) and the critical solid fraction (0.64) were estimated based on application of established theory to the iron-iron carbide binary phase diagram. In order to apply the generalized theory, it is necessary to have a eutectic phase transformation, so the phase diagram in the peritectic reaction region was approximated by a larger triangle, producing a region similar to a eutectic phase transformation. The coherent and critical temperature lines were proportionally drawn onto the modified binary iron-iron carbide binary phase diagram. Two intersection points with vertical lines passing through the liquidus and solidus temperatures were found to calculate the coherent solid fraction and the critical solid fraction using tie line and lever rules.

Gaussian Heat Input

Gaussian heat input was defined by the arc power and Gaussian heat distribution parameter as discussed previously. For the pulsed GMAW process, the instantaneous power calculated as the product of simultaneous current and voltage samples varies during the weld, so the instantaneous average power, 8842 W was calculated as the average of these values. This is larger than the actual energy deposited into the weld, so the actual power is adjusted by multiplying by the arc efficiency value measured by liquid nitrogen calorimetry (Ref. 43) as 0.74, which is typical of GMAW arc efficiencies measured by this technique. This actual power is still an average power, so the peak power and

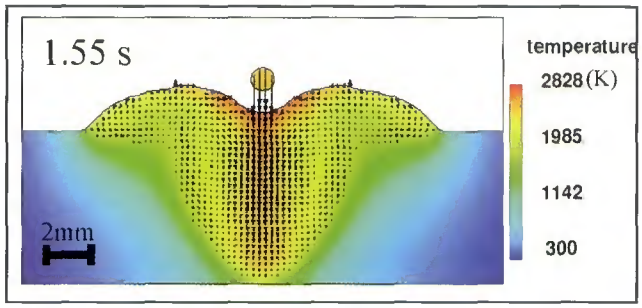

Fig. 18 — Cross-sectional view at 1.55 s for larger Lorentz force case showing complete penetration of the base material, finger-like penetration shape, and weak outward circulation at the weld pool edge.

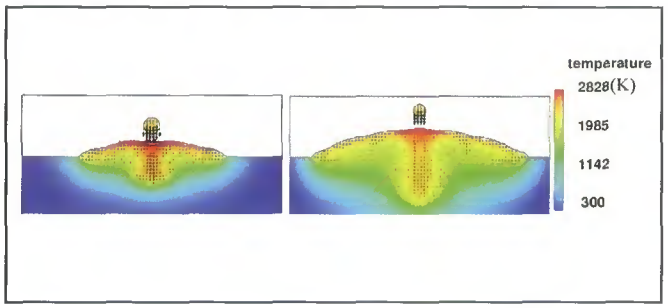

Fig. 19 — Cross-sectional views for decreased total force case at 0.5 and 1.7. Final weld penetration was decreased.

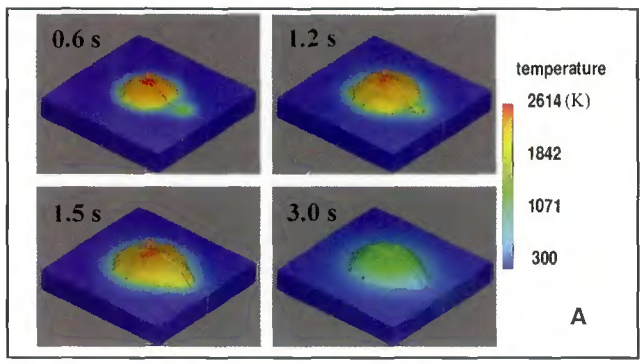

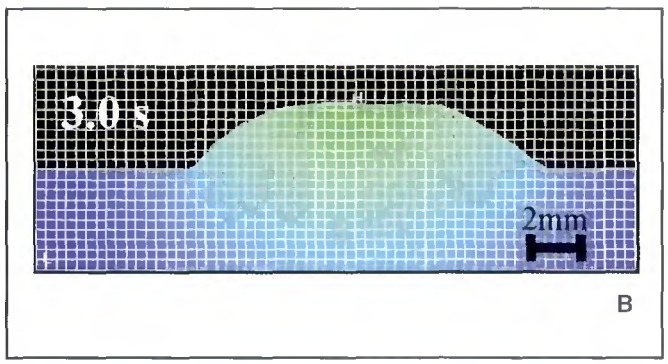

Fig. 20 — A — 3-D sequential images; B — cross section of two-heat sources simulation result. The additional heat is applied at the right edge of weld pool with 1-mm-radius laser beam.

the background power measured from current and voltage waveforms are used to represent the pulsing behavior of actual heat input during the weld, and then the actual power was further split to the arc power and the power consumed for molten drop generation.

To determine the heat input density distribution on the weld pool surface, the Gaussian heat distribution parameter for a direct heat input was estimated based on the empirical equation obtained from the literature (Ref. 34). This equation is a function of current for a 4-mm arc length case expressed as

$$\sigma_a = 0.533I^{0.2941} \qquad (22)$$

where σ_a is Gaussian heat distribution parameter (mm) and I is current (amps). Current measurements from the DAQ system were used to compute this value.

Arc Pressure, Drag Force, and Lorentz Force

From Equation 17, total arc force and Gaussian pressure distribution parameter are required to calculate the arc pressure on the weld pool. For the arc pressure computation, the current waveforms and the electrode tip angles were measured in order to estimate the arc pressure from literature formulas. According to the previous research papers (Refs. 4, 16), the empirical equations for the total force and Gaussian pressure distribution parameter as a function of current and electrode tip angle were expressed as

$$P = \begin{cases} -0.04017 + 0.0002553 \cdot I(N) & \text{(60-deg tip angle)} \\ -0.04307 + 0.0001981 \cdot I(N) & \text{(90-deg tip angle)} \end{cases} \qquad (23)$$

$$\sigma_p = \begin{cases} 1.4875 + 0.00123 \cdot I(mm) & \text{(60-deg tip angle)} \\ 1.4043 + 0.00174 \cdot I(mm) & \text{(90-deg tip angle)} \end{cases} \qquad (24)$$

where P is the total force (N), I is current (amps), and σ_p is Gaussian pressure distribution parameter (mm). The time-dependent current waveforms and electrode tip angles discussed previously were used in Equations 23 and 24 to compute these values.

The analytical solution (Ref. 36) for drag force calculation obtained from the literature requires Reynolds number and a ratio of jet height and nozzle diameter. The jet nozzle height was taken as 4 mm based on high-speed video arc length measurements and the jet diameter was set at 1 mm, approximately equal to the electrode diameter. Reynolds number contains the plasma jet velocity term that is computed using Bernoulli's equation based on the maximum arc pressure at the weld pool center computed from the arc pressure calculation at zero radius. Other terms involved in Reynolds number are the material properties of the plasma jet found from the literature (Ref. 44). The density and dynamic viscosity of argon plasma are 0.046 kg/m^3 and 0.00005 kg/m·s at 10,000 K plasma temperature.

The theoretical equation of Lorentz force in the weld pool derived based on the fixed boundary conditions except the free surface boundary condition. The current density distribution on the free surface is varying with time, so the input parameters to determine Lorentz force are pulse current and relative Gaussian current density parameters obtained from the previous research paper (Ref. 34). The empirical equation for Gaussian current density distribution parameter is expressed as

$$\sigma_c = 0.5342I^{0.2684} \qquad (25)$$

where σ_c is Gaussian current density distribution parameter (mm) and I is current (amps).

Drop Generation

For simulated drop generation, velocity, height, frequency, temperature, and drop radius were needed. Most of the parameters were obtained from analysis of video images, and drop temperature was set from literature values. In the simulation, molten drops were generated as spherical shape droplets.

There are two metal transfer behaviors seen in the video images in Fig. 1. For metal transfer at early weld times (before 1.2 s), the drop frequency was one drop per every two pulses, or a drop generation rate of 125 Hz, and drop velocity was 0.9 m/s at a distance 1.2 mm away from the weld pool surface. These values were measured from the metal transfer sequences observed in the high-speed video images shown in Fig. 5A. At weld times of 1.2 s and greater, metal transfer was more stable, and transfer rate was one drop per pulse, or a drop frequency of 250 Hz. Drop velocity was increased to 1.35 m/s, measured from the video images of metal transfer presented in Fig. 5B. The drop temperature for both transfer behaviors was set to be 2400 K from previous research reports (Ref. 40).

Results and Discussion

With simulation parameters determined from direct measurements and the literature, the simulation of pulsed GMA welding was conducted, and simulation results were validated with experimental results as detailed below.

Comparison of Final Weld Geometry

A very common way to validate weld simulations is to compare the dimensions of weld cross-sections measured from experiments with those predicted by the simulation. In Fig. 6, the actual weld cross-sectional images and the simulated cross-sectional weld views are displayed in order to compare reinforcement, radius, toe angles, and penetration. The quantitative comparison of the simulation and the experimental results is given in Table 3. Weld reinforcement measurements of the actual weld shown in Fig. 6A vary from 1.9 to 2.3 mm depending on the measuring locations (A and B). The average height, 2.1 mm, is comparable to the simulated weld height of 1.9 mm. There are two penetrations observed at the center and the edge of the weld shown in Fig. 6A. The inward circulation developed by drop momentum, arc pressure, and Lorentz force generates the center weld penetration, but the outward circulation induced by Marangoni force and plasma drag force produces the penetration at the weld edge. To compare weld penetrations, the simulation result at the weld termination time (1.8 s) when the maximum penetration occurs during the weld was used to measure the weld penetrations and the two clear circulations observed in Fig. 7.

In summary, differences in weld radius, the height of weld reinforcement, weld toe angles, and penetration at the edge are 10%, but the simulated weld penetration at the center is significantly deeper than the experimental measurement. This discrepancy is attributed to the high efficiency of drop momentum and heat transfer mainly due to fluid convection in the simulation. According to Fig. 8, metal transfer images show that molten droplets at the initial weld time up to 0.5 s were not spherical, and also the location of droplet impingement on the weld pool was somewhat random during the weld. Therefore, at the initial weld time before 0.5 s, the experimental weld pool was not yet as developed as the simulated one, and the weld metal convection that effectively transfers momentum and heat to the bottom of the weld pool was not as strong.

Sequential simulated weld cross-sectional images from 0.1 to 0.5 s are displayed to show the development of fluid flow at the early weld time in Fig. 9. In simulation, molten spherical droplets were generated at 1.2 mm above the weld surface at the center of the arc and traveled straight down to the base material every time. At 0.1-s simulation time, the molten metal deposited from the welding wire simply lays on the solid base material. The weld does not begin penetrating into the base material until 0.2 s. At around 0.3 s, the fluid flow in the weld pool is fully developed, weld penetration is enhanced, and clockwise and counterclockwise fluid flow circulations are also clearly observed at the edges and the center of the weld pool. The presence of two stable circulations in the weld pool is evidence of a stable weld pool. At 0.5 s, deeper penetration is observed along with larger fluid flow circulations.

From Fig. 9, it is concluded that the inward circulation is very significant to increase penetration at the center of the weld pool. This inward circulation is caused by drop momentum, arc pressure, and Lorentz force. First, the concentrated droplet impact onto the weld pool transfers their momentum along with their enthalpy (which is high) at the center of weld, promoting the inward circulation. The Gaussian arc pressure distribution generated by the arc plasma jet flow depresses the weld pool surface at the center, also enhancing the inward circulation. Additionally, at the high welding current, Lorentz body force adds to the inward circulation. The temperature distribution coloration of the images shows many red cells at the bottom center of the weld pool and a large temperature gradient at the solid/liquid interface, which accelerates melting of the solid phase. Therefore, it is proposed that the weld penetration in the simulation is deeper because the development of inward fluid flow circulation pattern in the simulation occurs earlier rather than in the experiment.

In Fig. 10, the simulated weld penetration vs. weld time is plotted to show the predicted transient weld penetration. As discussed before, the weld penetration is growing quickly due to the efficient drop momentum transfer and heat transfer when the fluid flow is fully developed. In the simulation, the fluid flow is fully developed at 0.2 s, so the slope of the weld penetration curve is steep except for the time between 0.8 and 1.1 s. The absorption of drop momentum depends on the thickness of the molten metal deposit, so the convexity of molten metal at 0.8 s is enough to absorb the drop momentum that stops penetration into the base material. After 1.2 s, the stronger arc pressure due to the transition to one drop per pulse mode depresses the weld pool surface to enhance the efficiency of drop momentum transfer into the weld pool, so the weld penetration increases from 1.2 s until the arc termination time. Interestingly, if the penetration curve is shifted to right about 0.5 s, which is the time for no penetration period due to the unstable metal transfer during the weld shown in Fig. 8, the final predicted weld penetration is 3.35 mm, which closely matches with the actual weld penetration of 3.2 mm.

This also suggests that the time to develop the inward circulation of fluid flow in the weld pool is related to the final weld penetration. Therefore, it is supposed that the random behavior of experimental metal transfer is a significant cause of the discrepancy between the predicted and experimental weld penetrations. Other simulation inputs related to the arc could also affect weld penetration, as will be discussed further below. Presumably, the discrepancy would be reduced if the computer model simulated the random behavior of metal transfer at the initial weld time.

Comparison of Transient Weld Pool Radius and Temperature

The numerical simulation of stationary GMAW-P was also validated by comparing the transient radius of weld deposits. In Fig. 11, the time-varying radius from high-speed video measurements and simulation predictions are plotted vs. weld time. One sample of captured im-

ages shown in Fig. 12 described that the weld pool radius is directly measured from the molten metal image using the electronic image of the ruler. According to both experimental and simulated results, the deposit radius increased rapidly at the beginning of the weld. This is presumed to correspond to rapid spreading of the solidus isotherm on the substrate surface by direct arc heating allowing spreading of the molten metal deposit. The spreading quickly transitions to a more gradual increase. At the later stage of spreading, heat conduction and convection are the main factors to increase the temperature at the liquid-solid junction to allow spreading of the molten metal. Of these two, heat conduction is usually considered to be less effective for heat transfer than thermal convection by fluid motion.

In the experimental deposit radius curve, the initial molten metal radius quickly reached 6.5 mm, which is a little bit larger than a visible arc radius (4 mm) estimated from the video images. The slope of the curve was still steep until the radius reached 6.5 mm, an observation that supports the explanation of the influence of direct arc heat input on the spreading of molten metal deposits. The experimental radius fluctuated at early times but is so less as the deposit grew larger. In the simulated radius curve, the deposit radius quickly increases up to 6.5 mm (about 0.6 s) due to the rapid direct heating from the arc. The time for the simulated weld deposit radius to reach the gradual increase stage and the radius itself are closely matched to experimental results, and the overall trend of the spreading behavior is almost identical between the experiment and the simulation.

Thermocouple measurements taken during welding were also used for simulation validation. In Fig. 13, three curves showing temperature history at a location 0.4 mm away from the final weld edge are plotted to compare the experimental and predicted thermal history. The difference between the two simulation curves is due to a small mesh domain (2.4×2.4 cm) and a large mesh domain (3×3 cm). Both simulation curves are closely matched with the experimental results until 1.5 s, but the small mesh domain results are considerably mismatched after 1.5 s due to an edge effect. This effect causes the temperature for the small mesh domain case to become too large after 1.5 s because heat transfer rate through the simulation boundary by natural convection is much smaller than heat conduction in the base material. Interestingly, the rate of temperature increase before 1.5 s is the same for both simulation cases because the conducted heat does not reach the computational boundary until this time.

Based on the temperature history validation, 3 cm is considered to be a sufficient computational domain size for the accurate computer simulation of the results over the time being considered. A sketch of the large simulation mesh mentioned in the preceding paragraph and used for subsequent simulations is provided in Fig. 14. This mesh consisted of 5 blocks with 132,400 cubical cells. The size of cells in the center block was 0.25 mm, allowing the accurate calculation of surface tension for molten droplets, while that of other blocks was 0.5 mm.

The simulations were run on a dual 3.4-GHz Xeon processor workstation with 2 GB of RAM, and the software was compiled dual process use. The computational time step, limited by the surface tension convergence criteria, was 2.3×10^{-5} s. Simulating 3 s of weld time required 62 h of "wall-clock" time. It was found that mesh size was most critical for accurate simulation of transferring droplets and the center block mesh size mentioned above was chosen for mesh size independent simulation of this aspect of the process.

Based on these three validations of the weld simulation, the stationary GMAW-P weld simulation was considered reasonably accurate for prediction of the final and transient weld profiles. In subsequent simulations, the Gaussian heat distribution parameter, Gaussian current distribution parameter, Gaussian pressure distribution parameter, and total arc pressure were individually varied to understand their effects on fluid and heat flow and weld pool penetration by comparing with validated simulation results.

Simulation Parameter Effects

The Gaussian heat distribution parameter was increased by a factor of 1.5 with same total heat input to study its effect on the weld profile and fluid flow patterns. The larger Gaussian heat distribution parameter corresponds to a broader heat distribution and less heat input intensity at the center of the arc, so it is expected that more time would be required to melt the base material underneath of the arc. According to the transient radius plots in Fig. 15, the weld deposit for the large heat input radius case did not spread as quickly as the validated simulation at initial times because the solid base material adjacent to the molten metal deposit was cooler. At later weld times, the weld pool radius was more well matched with the validated simulation deposit radius.

In Fig. 16, the effect of variation of the heat distribution parameter on the weld penetration transient weld penetration is shown. When the parameter was increased, the final weld penetration was decreased as expected because less energy was deposited at the center of weld pool and transferred to the bottom.

At the initial weld time shown in the cross-sectional view in Fig. 17A, no weld penetration was generated until 0. 2 s due to lower energy deposition from the arc. The weld began penetrating at 0.3 s due to heat conduction from the molten metal deposit and heat convection induced by several forces involved in the weld pool. After 0.3 s, the weld penetration is growing as fast as one for the validated simulation until 0.8 s weld time. The same penetration behavior (no penetration increase) was observed between 0.8 and 1.2 s compared to the validated simulation weld because the sufficient molten metal deposited absorbed drop momentum to prevent the penetration.

Again, the weld penetration is increasing after 1.2 s due to the increase of arc pressure depressed the weld pool surface, but it transitioned to a steady state at the end of a weld time due to the lower enthalpy transferring from the weld pool surface to the bottom of the weld. Figure 17B presented the low temperature of molten metal near the surface and at the bottom of weld pool compared to the validated simulation shown in Fig. 7B.

Lorentz force usually becomes the dominant factor at high welding current, so Gaussian current distribution parameter was reduced by the factor of half to study its effectiveness on the weld pool. The decrease of Gaussian current distribution parameter produces the constricted current flow through the weld pool, so the stronger Lorentz force is generated near the center of the weld pool. Due to the strong body force near the weld pool center, the strong inward circulation is expected to increase the weld penetration.

As shown in Fig. 18, weld penetration increased from 4.6 to 6.35 mm (thickness of plate), and the deep finger-like penetration shape is achieved.

Another interesting characteristic revealed by the flow vectors in this figure is the small counter fluid flow in the edge of the weld pool. Usually, Marangoni force produced by a negative surface tension gradient case and drag force generated by arc plasma jet force the fluid on the weld pool surface to flow outward, a direction that is against that induced by the Lorentz force. In this case, the Lorentz force was so strongly distributed near the weld pool center that it dominated the fluid flow pattern, producing a strong inward circulation of fluid flow. The transient weld penetration plotted in Fig. 16 shows that the slope of curve is steeper than other cases, and the weld penetrated through the base material at 1.55 s before the termination of the arc shown in Fig. 18.

One interesting point in this plot between 0.8 and 1.2 s is that the inward circulation mainly enhanced by the Lorentz force overcomes the barrier generated by the molten metal deposit as a momentum absorber so the weld penetration keeps increasing but it slows down. After 1.2 s, the slope is even steeper due to the combination of the increased arc pressure and high Lorentz force.

Figure 15 shows the transient radius of molten metal deposit. As discussed before, the outward circulation is mainly spreading the molten metal deposit, so the molten metal deposit is spreading as fast as the validated simulation until 0.5 s, but it slows down due to the small outward circulation at the edge of the weld pool shown in Fig. 18.

To demonstrate the effect of arc pressure, the total force and Gaussian pressure distribution parameter were individually varied while other simulation variables were held fixed. First, one fifth of arc force is applied to study because the arc pressure used in the simulation is strong enough to obtain a deep penetration. As discussed in the previous section, arc pressure and drag force are coupled together, so their magnitudes are proportional to each other. Therefore, the decrease of total force induces the weaker drag force. In Fig. 15, the trend of transient weld pool radius for the reduced arc pressure is showing no influence on the molten metal spreading. The weld penetration was plotted in Fig. 16. Before 1.3 s, the trend of weld penetration is following the validated simulation case, but at the later time the weld penetration is suddenly becoming steady. The final weld penetration is eventually decreased by 0.75 mm.

As discussed before, the inward circulation of fluid flow causes the increase of weld penetration. The magnitude of this circulation and the amount of enthalpy contained in molten metal are the main factors to determine the depth of weld penetration. Therefore, the stronger inward fluid flow circulation and the hotter molten metal accelerate the weld penetration. The amount of enthalpy in the molten metal on the weld pool surface is proportional to the arc direct heat deposit, so this factor is not required to consider the change of weld penetration as long as the same arc heat input distribution applied.

The mechanism to explain the decrease of final weld penetration can be described by the inward circulation of fluid flow. There are three forces involved to determine the magnitude of inward circulation. First, the lateral distribution of arc pressure causes the inward fluid flow so that the hot molten metal heated by the direct heat input to increase weld penetration. Second, metal transfer is a major source of heat and drop impact momentum to increase GMA weld penetration. Finally, Lorentz force at the high welding current induces the inward fluid flow to increase the weld penetration. During the weld, these forces are simultaneously acting on the weld pool to determine the magnitude of the inward fluid flow circulation.

In Fig. 19, there are two cross-sectional views at 0.5 and 1.7 s weld times displayed to explain the weld penetration characteristics during the weld. At the early weld time, there is not enough molten metal deposit to form the sufficient convexity of weld reinforcement acting as a damper to reduce the weld penetration even though the weak arc pressure was applied on the weld pool surface.

During the early weld time, Lorentz force and drop impact momentum are the dominant factors to increase the weld penetration. Molten metal eventually piled up as weld time goes on, so the amount of molten metal deposit on the substrate is sufficient enough to form the thick convexity to absorb the drop impact momentum displayed in Fig. 19. Therefore, the weld penetration is transitioned to a gradual increase as shown in Fig. 16.

Another variable to change the arc pressure distribution is a Gaussian pressure distribution parameter that increased by the factor of 1.5 with a fixed total force. The increase of this parameter decreases the maximum pressure and increases the area to apply. The transient weld pool radius and penetration were plotted in Figs. 15 and 16. The trend of transient weld pool radius is following the validated simulation, but the penetration curve is different from the validated simulation at the later weld time (after 1.2 s). Therefore, the final weld penetration is decreased to 3.6 mm due to the decrease of maximum arc pressure at the weld center.

In summary, the weld radius is not strongly influenced by simulation parameters except the Gaussian current distribution parameter, but the weld penetration is affected by all simulation parameters tested so far. According to previous demonstrations, it is not easy to modify the final weld profile, especially the spreading of molten metal, by given welding parameters demonstrated so far, thus the additional heat source such as a laser beam can be applied into the welding process in order to increase the controllability of the final weld shape during the weld.

Preliminary Demonstration of Additional Heat Source

Previous sections demonstrated how welding parameters could control the final weld shape, but in this section, the effect of the additional heat source that can enhance the controllability of the final weld shape is investigated. To improve the wetting characteristics of molten metal for the desired weld shape, the additional heat source such as laser beam is applied to demonstrate the controllability of the final weld shape using the numerical simulation as a tool.

For the demonstration of the improvement of molten metal wetting, the simulation of two heat sources is performed to show the effectiveness of additional heat source (it can be any heat source) adjacent to the edge of weld pool. The defocused laser beam as the second heat source was modeled to perform, and the results are shown in Fig. 20. According to Fig. 20, the molten metal wet over into the additional heat spot (laser spot), and it demonstrates the change of the final weld shape. Especially, the toe angle where the wetting occurred became smoother due to the additional heat source. Consequently, this preliminary test result using the 3-D numerical simulation as a process development tool can provide the insight for the process development of improving the controllability of the final weld shape for the further investigation.

Conclusions

The VOF technique was used to implement a simulation of stationary pulsed GMA welding that included nonisothermal free-surface fluid flow. Buoyancy, Marangoni, arc pressure, drag, and Lorentz forces were mathematically modeled and implemented in the numerical simulation. Pulsed gas metal arc size and droplet transfer were measured from arc images and used to determine some simulation variables. Direct comparisons of predicted and measured weld cross-section geometry, time-varying deposit radius, and temperature history from thermocouple measurements showed general agreement and validated the GMAW-P stationary welding simulation.

The weld penetrations predicted by simulation were somewhat deeper than the experimental measurements. This discrepancy was mainly attributed to the consistent droplet impact location in the simulations versus random droplet impact location in the experiments.

Simulation tests with individual changes of variables provided insight into the effects of these variables on fluid flow patterns and weld pool shape. When the radius of the distribution of current flow into the weld pool was decreased, the larger current density drastically increased the weld penetration but de-

creased the weld radius because it produced a dominant inward and downward circulation of weld metal.

Reduced total force and increased arc pressure distribution radius both decreased the weld penetration because they produced a weld deposit that was more convex, which absorbed the momentum of impinging droplets. Conversely, weld pools subjected to increased arc pressure and smaller pressure distribution were more concave at their center and thus had deeper penetration. Understanding of the effects of these variables on weld pool fluid flow and weld shapes provided key insights that are useful for future investigations that use the simulation as a tool to assist in weld process development.

Acknowledgments

Partial support of this work by EWI under contract 47412-GTO and ONR under contract N00014-05-1-0375 is acknowledged.

References

1. Nguten, T., and Wahab, M. 1995. A theoretical study of the effect of weld geometry parameters on fatigue crack propagation life. *Engineering Fracture Mechanics* 51: 1–18.

2. Choi, H. W., Farson, D. F., and Cho, M. H. 2006. Using a hybrid laser plus GMAW process for controlling the bead humping defect. *Welding Journal* 85: 174-s to 179-s.

3. Lu, M., and Kou, S. 1988. Power and current distributions in gas tungsten arc welding. *Welding Journal* 67(2): 29-s to 34-s.

4. Lin, M. L., and Eagar, T. W. 1986. Pressures Produced by Gas Tungsten Arcs. *Met. Mat. Trans.* 17B: 601–607.

5. Adonyi, Y., Richardson, R., and Baselack III, A. 1988. Investigation of arc force effects in subsurface GTA welding. *Welding Journal* 71(9): 321-s to 330-s.

6. Tanaka, M., Ushio, M., and Lowke, J. J. 2003. Time dependent numerical analysis of stationary GTA welding process. *Trans. JWRI* 32(2): 259–263.

7. Heiple, C. R., and Roper, J. R. 1982. Mechanism for minor element effect on GTA fusion zone geometry. *Welding Journal* 61(4): 97-s to 102-s.

8. Heiple, C. R., and Burgardt, P. 1985. Effects of SO_2 shielding gas additions on GTA weld shape. *Welding Journal* 64(6): 159-s to 162-s.

9. Joos, G. 1934. *Theoretical Physics*, 3rd Ed. p. 224, Blackie and Son, Glasgow, Scotland.

10. Matsunawa, A., and Ohji, T. 1982. Role of surface tension in fusion welding (Part 1). *Trans. JWRI* 11(2): 145–154.

11. Matsunawa, A., and Ohji, T. 1983. Role of surface tension in fusion welding (Part 2). *Trans. JWRI* 12(1): 123 to 130.

12. Lin, M. L., and Eagar, T. W. 1985. Influence of arc pressure on weld pool geometry. *Welding Journal* 64(6): 163-s to 169-s.

13. Kim, J.-W., and Na, S.-J. 1995. A Study on the effect of contact tube-to-workpiece distance on weld pool shape in gas metal arc welding. *Welding Journal* 74(5): 141-s to 152-s.

14. Cho, S.-H., and Kim, J.-W. 2001. Thermal analysis of horizontal fillet joints by considering bead shape in gas metal arc welding. *Sci. Technol. Weld. Joining.* 6(4): 220–224.

15. Kim, C. H., Zhang, W., and DebRoy, T. 2003. Modeling of temperature field and solidified surface profile during gas-metal arc fillet welding. *J. of Appl Phys.* 94: 2667–2679.

16. Zhang, W., Kim, C. H., and DebRoy, T. 2004. Heat and fluid flow in complex joints during gas metal arc welding — Part I: Numerical model of fillet welding. *J. of Appl Phys.* 95: 5210-5219.

17. Zhang, W., Kim, C. H., and DebRoy, T. 2004. Heat and fluid flow in complex joints during gas metal arc welding — Part II: Application to fillet welding of mild steel. *J. of Appl Phys.* 95: 5220–5229.

18. Kumar, A., and DebRoy, T. 2004. Guaranteed fillet weld geometry from heat transfer model and multivariable optimization. *Int. J. of Heat and Mass Transfer* 47: 5793–5806.

19. Trapaga, G., and Szekely, J. 1991. Mathematical modeling of the isothermal impingement of liquid droplets in spraying processes. *Met. Mat. Trans.* 22B: 901–914.

20. Zheng, L. L., and Zhang, H. 2000. An adaptive level set method for movin-boundary problems: Application to droplet spreading and solidification. *Numer Heat Tr B-Fund.* 41: 437–454.

21. Wang, Y., and Tsai, H. L. 2001. Impingement of filler droplets and weld pool dynamics during gas metal arc welding process. *Int. J. of Heat and Mass Transfer* 44: 2067–2080.

22. Chiang, K. C., and Tsai, H. L. 1992. Shrinkage-induced fluid flow and domain change in two-dimensional alloy solidification. *Int. J. of Heat and Mass Transfer* 35: 1763–1770.

23. Haidar, J., and Lowke, J. J. 1996. Predictions of metal droplet formation in arc welding. *J. Phys. D: Appl Phys.* 29: 2951–2960.

24. Haidar, J. 1998. A theoretical model for gas metal arc welding and gas tungsten arc welding. *I. J. of Appl Phys.* 84: 3518 –3529.

25. Haidar, J. 1998. Predictions of metal droplet formation in gas metal arc welding. II. *J. of Appl Phys.* 84: 3530–3540.

26. Wang, G., Huang, P. G., and Zhang, Y. M. 2003. Numerical analysis of metal transfer in gas metal arc welding. *Met. Mat. Trans.* 34B: 345–353.

27. Wang, F., Hou, W. F., Hu, S. J., Kannatey-Asibu, E., and Schultz, W. W. 2003. Modelling and analysis of metal transfer in gas metal arc welding. *J. Phys. D: Appl Phys.* 36: 1143–1152.

28. Quinn, T. P., Szanto, M., Gilad, I., and Shai, I. 2005. Coupled arc and droplet model of GMAW. *Science and Technology of Welding and Joining* 10: 113–119.

29. Fan, H. G., and Kovacevic, R. 2004. A unified model of transport phenomena in gas metal arc welding including electrode, arc plasma and molten pool. *J. Phys. D: Appl Phys.* 37: 2531–2544.

30. Hirt, C. W., and Nichols, B. D. 1981. Volume of fluid (VOF) method for the dynamics of free boundaries. *J. Comp. Phys.* 39: 201–225.

31. Carman, P. C. 1937. Fluid flow through granular beds. *Trans. Inst. Chem. Engrs. 15: 150–166.*

32. Whitaker, S. 1986. Flow in porous media I: A theoretical derivation of Darch's law. *Transport in Porous Media 1: 3–25.*

33. Voller, V. R., and Prakash, C. 1987. A fixed grid numerical modeling methodology for convection-diffusion mushy region phase-change problems. *Int. J. Heat Mass Transfer* 30(8): 1709–1719.

34. Tsai, N. S., and Eagar, T. W. 1985. Distribution of the heat and current fluxes in gas tungsten arcs. *Met. Mat. Trans.* 16B: 841–845.

35. Sahoo, P., Debroy, T., and McNallan, M. 1988. Surface tension of binary metal-surface active solute systems under conditions relevant to welding metallurgy. *Met. Mat. Trans.* 19B: 483– 491.

36. Phares, D. J., Smedley, G. T., and Flagan, R. C. 2000. The wall shear stress produced by the normal impingement of a jet on a flat surface. *J. Fluid Mech.* 418: 351–375.

37. Kou, S., and Sun, D. K. 1985. Fluid flow and weld penetration in stationary arc welds. Met. *Mat. Trans.* 16A: 203–213.

38. Kumar, A., and DebRoy, T. 2003. Calculation of three-dimensional electromagnetic force field during arc welding. *J. of Appl Phys.* 94: 1267–1277.

39. Anon. 2003. Computer Code Flow-3D. Flow Science Corp, Los Alamos, N.Mex.

40. Jones, L. A., Eagar, T. W., and Lang, J. H. 1985. Investigation of drop detachment control in gas metal arc welding. MIT: 1009–1013.

41. Essers, W. G., and Walter, R. 1981. Heat transfer and penetration mechanisms with GMA and plasma-GMA welding. Welding Journal 60(2): 37-s to 42-s.

42. Borland, J. C. 1960. Generalized theory of super-solidus cracking in welds (and castings). *Br. Weld. J.* 7: 508–512.

43. Joseph, A., Harwig, D., Farson, D., and Richardson, R. 2003. Measurement and calculation of P-GMAW arc power and heat transfer efficiency. *Science and Technology of Welding and Joining* 8(6): 400–406.

44. Rat, V., Antre, P., Aubreton, J., Elchinger, M., Fauchais, P., and Vacher, D. 2002. Transport coefficients including diffusion in a two-temperature argon plasma. *J. Phys. D:Appl. Phys.* 35: 981–991.